Assessing the simulated soil thermal regime from Noah-MP LSM v1.1 for near-surface permafrost modeling on the Qinghai-Tibet Plateau

Xiangfei Li[1,2], Tonghua Wu[1,*], Xiaodong Wu[1], Xiaofan Zhu[1], Guojie Hu[1], Ren Li[1], Yongping Qiao[1], Cheng Yang[1,2], Junming Hao[1,2], Jie Ni[1,2], Wensi Ma[1,2]

[1] Cryosphere Research Station on the Qinghai-Tibet Plateau, State Key Laboratory of Cryospheric Science, Northwest Institute of Eco-Environment and Resources, Chinese Academy of Sciences, Lanzhou 730000, China

[2] University of Chinese Academy of Sciences, Beijing 100049, China

Correspondence: Tonghua Wu (thuawu@lzb.ac.cn)

Abstract. Land surface models (LSMs) are effective tools for near-surface permafrost modeling. Extensive and rigorous model inter-comparison is of great importance before application due to the uncertainties in current LSMs. This study designed an ensemble of 6912 experiments to evaluate the Noah land surface model with multi-parameterization (Noah-MP) for soil temperature (ST) and soil liquid water (SLW) simulation, and investigate the sensitivity of parameterization schemes at a typical permafrost site on the Qinghai-Tibet Plateau. The results showed that Noah-MP systematically overestimates snow cover and thus induces great cold bias in ST. After removing the snow process, the cold bias remain, especially during the cold season. And the uncertainty of ST is greater in the cold season (October-April) and for the deep soil layers. ST is most sensitive to surface layer drag coefficient (SFC) while largely influenced by runoff and groundwater (RUN). By contrast, the influence of canopy stomatal resistance (CRS) and soil moisture factor for stomatal resistance (BTR) on ST is negligible. With limited impacts on ST simulation, vegetation model (VEG), canopy gap for radiation transfer (RAD) and snow/soil temperature time scheme (STC) are more influential on shallow ST, while super-cooled liquid water (FRZ), frozen soil permeability (INF) and lower boundary of soil temperature (TBOT) have greater impacts on deep ST. In addition, Noah-MP generally underestimates soil moisture. The RUN process dominates the SLW simulation in comparison of the very limited impacts of all other physical processes. Furthermore, an optimal configuration of Noah-MP for permafrost modeling were extracted based on the connectivity between schemes, and they are: table leaf area index with calculated vegetation fraction, Jarvis scheme for CRS, Noah scheme for BTR, BATS model for RUN, Chen97 for SFC, zero canopy gap for RAD, variant freezing-point depression for FRZ, hydraulic parameters defined by soil moisture for INF, ST at 8 m for TBOT, and semi-implicit method for STC. The analysis of the model structural uncertainties and characteristics of each scheme would be constructive to a better understanding of the land surface processes on the QTP and further model improvements towards near-surface permafrost modeling using the LSMs.

1 Introduction

The Qinghai-Tibet Plateau (QTP) hosts the world's largest high-altitude permafrost covering a contemporary area of 1.06×10^6 km^2 (Zou et al., 2017). Under the background of climate warming and intensifying human activities, permafrost on the QTP has been widely suffering thermal degradation (Ran et al., 2018), resulting in reduction of permafrost extent, disappearing of permafrost patches and thickening of active layer (Chen et al., 2020). Moreover, such degradation could cause alterations in hydrological cycles (Zhao et al., 2019; Woo, 2012), changes on ecosystem (Fountain et al., 2012; Yi et al., 2011) and damages to infrastructures (Hjort et al., 2018). Therefore, it is very important to monitor and simulate the state of permafrost to adapt to the degradation.

Soil temperature (ST) is an intuitive indicator to evaluate the thermal state of permafrost. A number of monitoring sites have been established on the QTP (Cao et al., 2019). However, it is inadequate to construct the thermal state of permafrost by considering the spatial variability of the ground thermal regime and an uneven distribution of these observations. In contrast, numerical models are competent alternatives. In recent years, land surface models (LSMs), which describe the exchanges of heat, water, and momentum between the land and atmosphere (Maheu et al., 2018), have received significant improvements in the representation of permafrost and frozen ground processes (Koven et al., 2013; Nicolsky et al., 2007; Melton et al., 2019). LSMs are capable of simulating the transient change of permafrost by describing subsurface hydrothermal processes (e.g. soil temperature and moisture) with soil heat conduction (-diffusion) and water movement equations (Daniel et al., 2008). Moreover, they can be integrated with the numerical weather prediction system like WRF (Weather Research and Forecasting), making them as effective tools for comprehensive interactions between climate and permafrost (Nicolsky et al., 2007).

Some LSMs have been applied to modeling permafrost in the QTP. Guo and Wang (2013) investigated near-surface permafrost and seasonally frozen ground states as well as their changes using the Community Land Model, version 4 (CLM4). Hu et al. (2015)

applied the coupled heat and mass transfer model to identify the hydrothermal characteristics of the permafrost active layer in the Qinghai-Tibet Plateau. Using an augmented Noah LSM, Wu et al. (2018) modeled the extent of permafrost, active layer thickness, mean annual ground temperature, depth of zero annual amplitude and ground ice content on the QTP in 2010s. Despite those achievements based on different models, LSMs are in many aspects insufficient for permafrost modeling. For one thing, large uncertainties still exist in the state-of-the-art LSMs when simulating the soil hydrothermal regime on the QTP (Chen et al., 2019). For instance, 19 LSMs in CMIP5 overestimate snow depth over the QTP (Wei and Dong, 2015), which could result in the variations of the soil thermal regime in the aspects of magnitude and vector (cooling or warming) (Zhang, 2005). Moreover, most of the existing LSMs are not originally developed for permafrost modeling. Many of their soil processes are designed for shallow soil layers (Westermann et al., 2016), but permafrost may occur in the deep soil. And the soil column is often considered homogeneous, which can not represent the stratified soil common on the QTP (Yang et al., 2005). Given the numerous LSMs and possible deficiencies, it is necessary to assess the parameterization schemes for permafrost modeling on the QTP, which is helpful to identify the influential sub-processes, enhance our understanding of model behavior, and guide the improvement of model physics (Zhang et al., 2016).

Noah land surface model with multi-parameterization (Noah-MP) provides a unified framework in which a given physical process can be interpreted using multiple optional parameterization schemes (Niu et al., 2011). Due to the simplicity in selecting alternative schemes within one modeling framework, it has been attracting increasing attention in inter-comparison work among multiple parameterizations at point and watershed scales (Hong et al., 2014; Zheng et al., 2017; Gan et al., 2019; Zheng et al., 2019; Chang et al., 2020; You et al., 2020). For example, Gan et al. (2019) carried an ensemble of 288 simulations from multi-parameterization schemes of six physical processes, assessed the uncertainties of parameterizations in Noah-MP, and further revealed the best-performing schemes for latent heat, sensible heat and terrestrial water storage simulation over ten watersheds in China. You et al. (2020) assessed the performance of Noah-MP in simulating snow process at eight sites over distinct snow climates and identified the shared and specific sensitive parameterizations at all sites, finding that sensitive parameterizations contribute most of the uncertainties in the multi-parameterization ensemble simulations. Nevertheless, there is little research on the inter-comparison of soil thermal processes toward permafrost modeling. In this study, an ensemble experiment of totally 6912 scheme combinations was conducted at a typical permafrost monitoring site on the QTP. The simulated soil temperature (ST) of Noah-MP model was assessed and the sensitivities of parameterization schemes at different depths were further investigated. Considering the general performance and sensitive schemes of Noah-MP, we further explored the interactions between the most influential schemes and configured an optimal combination based on the connections between schemes. We hope this study can provide a reference for permafrost simulation on the QTP.

This article is structured as follows: Section 2 introduces the study site, atmospheric forcing data, design of ensemble simulation experiments, and sensitivity analysis and optimal selection methods. Section 3 describes the ensemble simulation results of ST, explores the sensitivity and interactions of parameterization schemes, and determines the optimal combination for permafrost modeling. Section 4 discusses the schemes in each physical process and proposes further research topics. Section 5 concludes the main findings of this study.

2 Methods and materials

2.1 Site description and observation datasets

Tanggula observation station (TGL) lies in the continuous permafrost regions of Tanggula Mountain, central QTP (33.07°N, 91.93°E, Alt.: 5,100 m a.s.l; Fig. 1). This site a typical permafrost site on the plateau with sub-frigid and semiarid climate (Li et al., 2019), filmy and discontinuous snow cover (Che et al., 2019), sparse grassland (Yao et al., 2011), coarse soil (Wu and Nan, 2016; He et al., 2019), and thick active layer (Luo et al., 2016), which are common features in the permafrost regions of the plateau. According to the observations from 2010–2011, the annual mean air temperature of TGL site was −4.4 °C. The annual precipitation was 375 mm, and of which 80% is concentrated between May and September. Alpine steppe with low height is the main land surface, whose coverage range is about 40% ~ 50% (Yao et al., 2011). The active layer thickness is about 3.15 m (Hu et al., 2017).

The atmospheric forcing data, including wind speed/direction, air temperature/relative humidity/pressure, downward shortwave/longwave radiation, and precipitation, were used to drive the model. These variables above were measured at a height of 2 m and covered the period from August 10, 2010 to August 10, 2012 (Beijing time) with a temporal resolution of 1 hour. Daily soil temperature and liquid moisture at depths of 5cm, 25cm, 70cm, 140cm, 220cm and 300cm from October 1, 2010 to September 30, 2011 (Beijing time) were utilized to validate the simulation results.

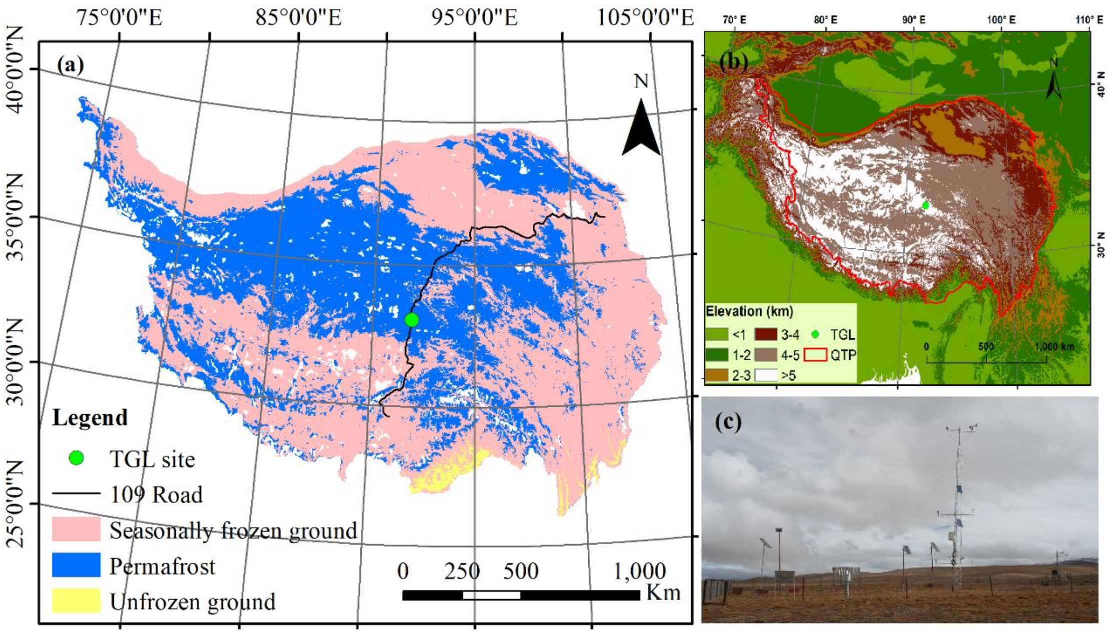

Figure 1. Location and geographic features of study site. (a) Location of observation site and permafrost distribution (Zou et al., 2017). (b) Topography of the Qinghai-Tibet Plateau. (c) Photo of the Tanggula observation station.

2.2 Ensemble experiments of Noah-MP

The offline Noah-MP LSM v1.1 was assessed in this study. It consists of 12 physical processes that are interpreted by multiple optional parameterization schemes. These sub-processes include vegetation model (VEG), canopy stomatal resistance (CRS), soil moisture factor for stomatal resistance (BTR), runoff and groundwater (RUN), surface layer drag coefficient (SFC), super-cooled liquid water (FRZ), frozen soil permeability (INF), canopy gap for radiation transfer (RAD), snow surface albedo (ALB), precipitation partition (SNF), lower boundary of soil temperature (TBOT) and snow/soil temperature time scheme (STC) (Table 1). Details about the processes and optional parameterizations can be found in Yang et al. (2011a).

In this study, the dynamic vegetation option in VEG process was turned off for simplicity. Previous studies has confirmed that Noah-MP seriously overestimate the snow depth on the QTP (Li et al., 2020; Wang et al., 2020). However, the impact of snow cover on ground temperatures in the permafrost regions of QTP is usually considered weak (Jin et al., 2008; Wu et al., 2018), because the snow cover is thin, short-lived, and patchy-distributed (Che et al., 2019). For practical purpose, the ALB and SNF processes were not considered by setting the snow fraction in precipitation to zero. Since no snow cover in the ground, the ground albedo equals the soil albedo. As a result, in total 6912 combinations are possible for the left 10 processes and orthogonal experiments were carried out to evaluate their performance in soil thermal dynamics and obtain the optimal combination.

The monthly leaf area index (LAI) was derived from the Advanced Very High-Resolution Radiometer (AVHRR) (https://www.ncei.noaa.gov/data/, Claverie et al., 2016). The Noah-MP model was modified to consider the vertical heterogeneity in the soil profile by setting the corresponding soil parameters for each layer. The soil hydraulic parameters, including the porosity, saturated hydraulic conductivity, hydraulic potential, the Clapp-Hornberger parameter b, field capacity, wilt point, and saturated soil water diffusivity, were determined using the pedotransfer functions proposed by Hillel (1980), Cosby et al. (1984), and Wetzel and Chang (1987)

(Equations S1-S7), in which the sand and clay percentages were based on Hu et al., (2017) (Table S1). In addition, the simulation depth was extended to 8.0 m to cover the active layer thickness of the QTP. The soil column was discretized into 20 layers, whose depths follow the default scheme in CLM 5.0 (Table S1, Lawrence et al., 2018). Due to the inexact match between observed and simulated depths, the simulations at 4cm, 26cm, 80cm, 136cm, 208cm and 299cm were compared with the observations at 5cm, 25cm, 70cm, 140cm, 220cm and 300cm, respectively. A 30-year spin-up was conducted in every simulation to reach equilibrium soil states.

Table 1. The physical processes and options of Noah-MP. Options in bold are the optimal selections in this study.

Physical processes	**Options**
Vegetation model (VEG)	(1) table LAI, prescribed vegetation fraction
	(2) dynamic vegetation
	(3) table LAI, calculated vegetation fraction
	(4) table LAI, prescribed max vegetation fraction
Canopy stomatal resistance (CRS)	**(1) Jarvis**
	(2) Ball-Berry
Soil moisture factor for stomatal resistance (BTR)	**(1) Noah**
	(2) CLM
	(3) SSiB
Runoff and groundwater (RUN)	(1) SIMGM with groundwater
	(2) SIMTOP with equilibrium water table
	(3) Noah (free drainage)
	(4) **BATS (free drainage)**
Surface layer drag coefficient (SFC)	(1) Monin-Obukhov (M-O)
	(2) Chen97
Super-cooled liquid water (FRZ)	(1) generalized freezing-point depression
	(2) Variant freezing-point depression
Frozen soil permeability (INF)	**(1) Defined by soil moisture, more permeable**
	(2) Defined by liquid water, less permeable
Canopy gap for radiation transfer (RAD)	(1) Gap=F(3D structure, solar zenith angle)
	(2) Gap=zero
	(3) Gap=1-vegetated fraction
Snow surface albedo (ALB)	(1) BATS
	(2) CLASS
Precipitation partition (SNF)	(1) Jordan91
	(2) BATS: $T_{sfc} < T_{frz}+2.2K$
	(3) $T_{sfc} < T_{frz}$
Lower boundary of soil	(1) zero heat flux

temperature (TBOT)	**(2) soil temperature at 8m depth**
Snow/soil temperature time scheme (STC)	**(1) semi-implicit** (2) full implicit

BATS (Biosphere–Atmosphere Transfer Model); CLASS (Canadian Land Surface Scheme); SIMGM (Simple topography-based runoff and Groundwater Model); SIMTOP (Simple Topography-based hydrological model); SSiB (Simplified Simple Biosphere model).

2.3 Methods for sensitivity analysis

The root mean square error (RMSE) between the simulations and observations were adopted to evaluate the performance of Noah-MP. The averages of the RMSEs of all the soil layers were defined as column RMSE (colRMSE).

To investigate the influence degrees of each physical process on ST and SLW, we firstly calculated the mean RMSE ($\bar{Y}_j^i$) of the *j*th parameterization schemes (*j* = 1, 2, …) in the *i*th process (i = 1, 2, …). Then, the maximum difference of $\bar{Y}_j^i$ ($\Delta\overline{RMSE}$) was defined to quantify the sensitivity of the *i*th process (*i* = 1, 2, …) (Li et al., 2015):

$$\Delta\overline{RMSE} = \bar{Y}_{max}^i - \bar{Y}_{min}^i$$

where $\bar{Y}_{max}^i$ and $\bar{Y}_{min}^i$ are the largest and the smallest $\bar{Y}_j^i$ in the *i*th process, respectively. For a given physical process, a high $\Delta\overline{RMSE}$ signifies large difference between parameterizations, indicating high sensitiveness of the *i*th process.

The sensitivities of physical processes were determined by quantifying the statistical distinction level of performance between parameterization schemes. The Independent-sample T-test (2-tailed) was adopted to identify whether the distinction level between two schemes is significant, and that between three or more schemes was tested using the Tukey's test. Tukey's test has been widely used for its simple computation and statistical features (Benjamini, 2010). The detailed descriptions about this method can be found in Zhang et al. (2016), Gan et al. (2019), and You et al. (2020). A process can be considered sensitive when the schemes show significant difference. Moreover, schemes with small mean RMSE were considered favorable for ST/SLW simulation. We distinguished the differences of the parameterization schemes at 95%

confidence level.

2.4 Optimal selection methods

To extract the optimal combinations of parameterization schemes, the connection frequency (CF) between parameterizations was calculated:

(1) Sorting the 6912 colRMSEs in an ascending order;

(2) Donating the colRMSEs concentrated below the 5th percentile as the "best combinations" (346 members);

(3) Counting the times of a given parameterizations occurring with other parameterizations in the "best combinations";

(4) The CF was then determined by dividing 346.

Obviously, for two given parameterization schemes, a large CF has an advantage in terms of optimal combination.

3 Results

3.1 General performance of the ensemble simulation

3.1.1 Snow process simulation

The performance of Noah-MP for snow simulation and its impacts on soil temperature was firstly tested by conducting an ensemble of 41472 (= 6912*2*3) experiments. Due to a lack of snow depth measurements, ground albedo was used as an indicator for snow cover. Figure 1 shows the monthly variations of observed ground albedo and the simulations produced by the ensemble simulations considering snow-related physical processes (i.e. the ALB and SNF processes). The ground albedo was extremely overpredicted with large uncertainties when considering the snow options in Noah-MP, indicating the overestimation of snow depth and duration. As a result, the soil temperature basically presented a huge cold bias and large uncertainties at all layers (Fig. S1). When neglecting the snow, the simulated ground albedo was nearer to the observation with a mean absolute error of 0.06. And the underestimation and uncertainties of soil temperature was greatly resolved.

The influence of snow cover on soil temperature was further analyzed based on in-situ measurements. Figure 3 shows the meteorological conditions and soil temperatures during a long-term snow process from 12/28/2010 – 1/27/2011. It can be seen that shallow soil temperature (5cm, 25cm, and 70cm) basically fluctuated with air temperature. At the beginning of the snow events on 1/1/2011, soil temperature at 5cm, 25cm, and 70cm was slightly increased by 1.5°C, 1.2°C, and 0.7 °C, respectively. With the melting of snow, the amplitude of soil temperature decreased. Meanwhile, soil temperature at deep layers showed no obvious fluctuations during the whole period. It indicates that snow cover at TGL site has a very limited effect on soil temperature, especially that of deep layers.

Given the poor simulation of Noah-MP for snow cover and the weak impact of snow on soil temperature in reality, we will focus on the results of ensemble simulations without considering snowfall (6912 experiments in total) in the following sections.

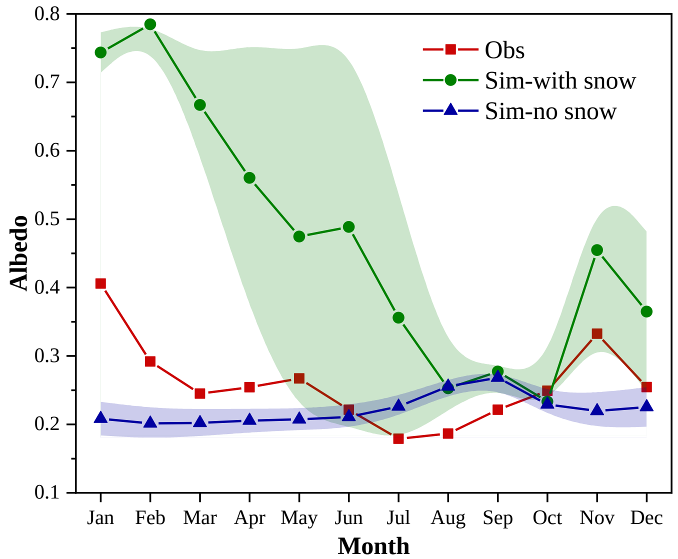

Figure 2. Monthly variations ground albedo at TGL site for observation (Obs), the ensemble simulation considering snow (Sim-with snow), and ensemble simulation neglecting snow (Sim-no snow). The green shadow represents the standard deviation of the ensemble simulation.

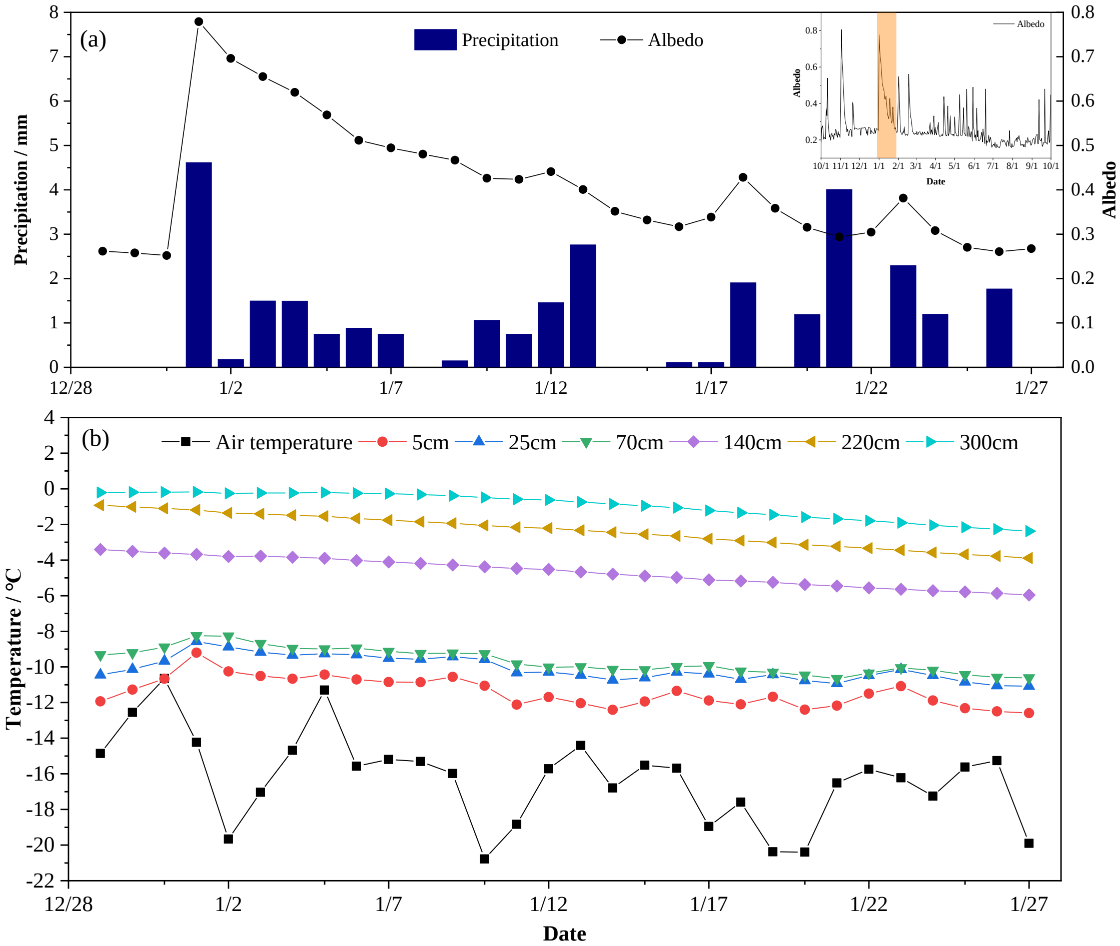

Figure 3. Variations of (a) precipitation and ground albedo, (b) air temperature and soil temperature at TGL site from 28 December 2010 to 27 January 2011.

3.1.2 Soil temperature and moisture simulation

We evaluated ST from the 6912 experiments against observations. Figure. 4 illustrates the ensemble simulated and observed annual cycle of ST at TGL site. The plots give the uncertainty ranges of the ensemble experiments using five statistical indicators, i.e., the first/third quartile (Q1/Q3), mean, the lower (Q1-1.5(Q3-Q1)) and upper bound (Q3+1.5(Q3-Q1)). The kernel density distribution of the simulated ST is also illustrated. The ensemble experiments basically captured the seasonal variability of ST, whose magnitude decreased with soil depth. In addition, the simulated ST in the cold season (October-April) showed relatively wide uncertainty ranges, particularly at the deep layers. This indicates that the selected schemes perform more differently during the cold season, which is especially so at the deep layers. The simulated ST were generally smaller than the observations with relatively large gap during the cold season.

It indicates that the Noah-MP model generally underestimates the ST, especially during the cold season. Moreover, the simulated ST was widely found to be bimodal distribution across the soil column, implying that two schemes dominate the ST simulation in the Noah-MP model.

Since the observation equipment can only record the liquid water, soil liquid water (SLW) was evaluated against simulations from the 6912 experiments (Fig. 5). The Noah-MP model generally underestimated surface (5cm and 25cm) and deep (300cm) SLW (Fig. 5g, 5h, 5l). However, Noah-MP tended to overestimate the SLW at the middle layers of 70cm, 140cm and 220cm. Moreover, the simulated SLW exhibited relatively wide uncertainty ranges during the warm season, particularly at the middle layers (Fig. 5). In addition, the distribution of the simulated SLW showed distinct bimodal peaks at the depth of 70cm and 140cm.

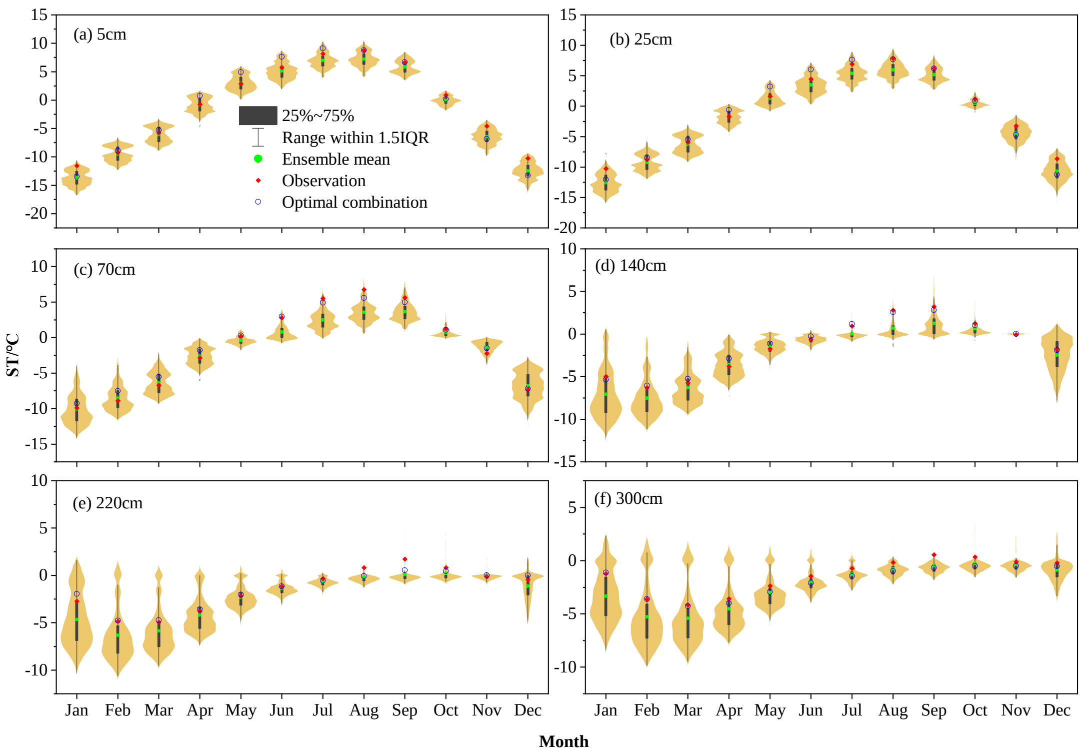

Figure 4. Monthly soil temperature (ST) at (a) 5 cm, (b) 25 cm, (c) 70 cm, (d) 140 cm, (e) 220 cm, (f) 300 cm at TGL site. Limits of the boxes represent upper and lower quartiles, whiskers extend to 1.5 times the interquartile range (IQR). The green circles in the box are the ensemble mean values. The light orange shading represents the kernel density distribution of simulated ST. The red diamonds are observations and the blue

circles are the results of the optimal scheme combination.

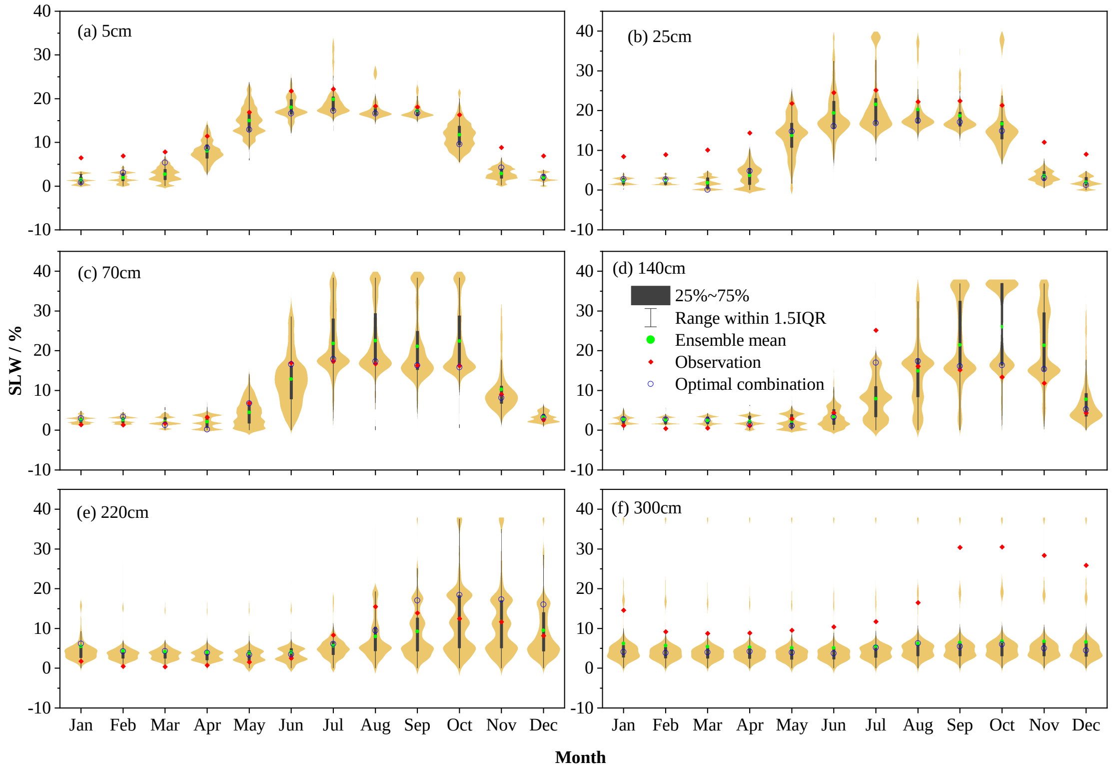

Figure 5. Same as in Figure 4 but for SLW.

3.2 Sensitivity of physical processes

3.2.1 Influence degrees of physical processes

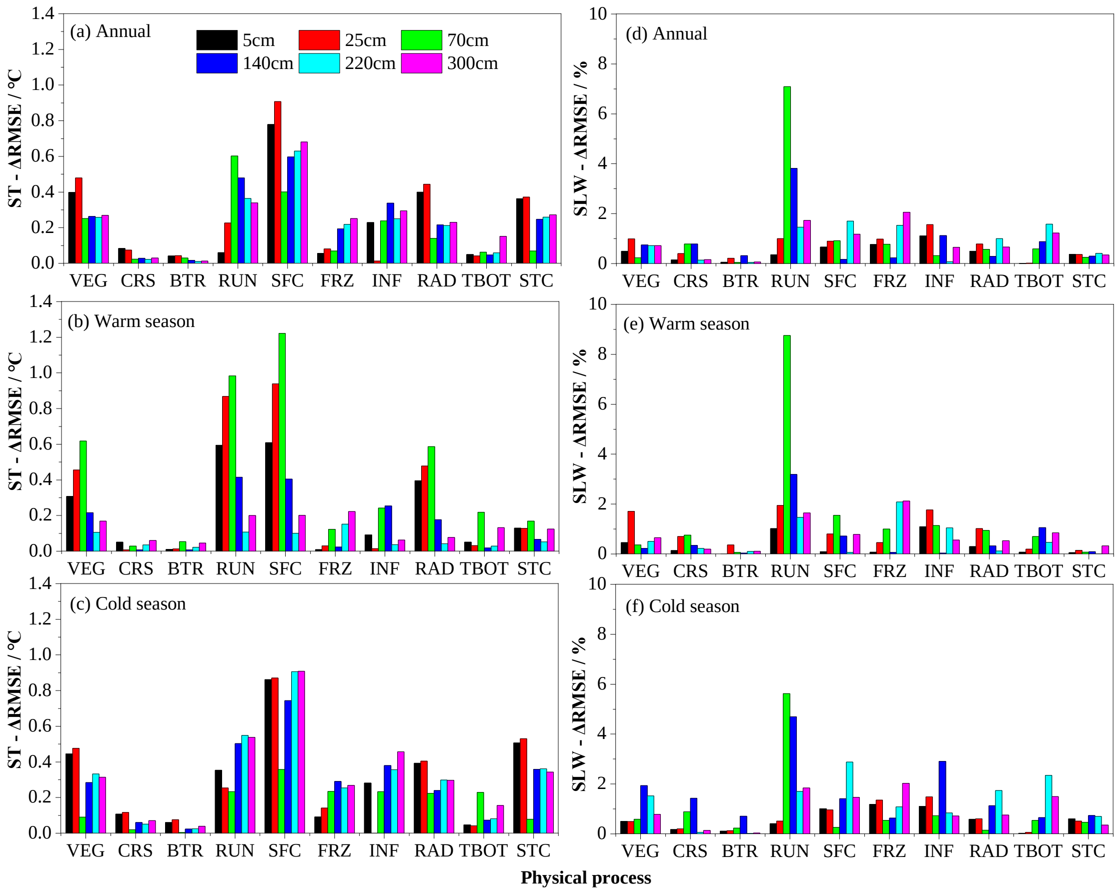

Figure 6. The maximum difference of the mean RMSE for (a, b and c) soil temperature (ST-$\Delta\overline{RMSE}$ in °C) and (d, e and f) soil liquid water (SLW-$\Delta\overline{RMSE}$ in %) in each physical process during the (a and d) annual, (b and e) warm season, and (c and f) cold season at different soil depths.

Figure. 6 compares the influence scores of the 10 physical processes at different soil depths, based on the maximum difference of the mean RMSE over 6912 experiments using the same scheme, for ST and SLW at TGL site. The SFC and RUN processes dominated the ST-$\Delta\overline{RMSE}$ at all layers, indicating that they are the most sensitive processes for ST simulation. While most of the ST-$\Delta\overline{RMSE}$ of the other 8 physical processes were less than 0.6°C, among which the influence of CRS and BTR processes were negligible. What's more, the VEG, RAD and STC processes were more influential on the shallow STs than the deep STs. Taking the RAD process as an example, the annual ST-$\Delta\overline{RMSE}$ of the 5cm and 25 cm were nearly 0.4°C while that of the 70 cm, 140cm, 220cm and 300cm were around 0.2°C. In contrast, the influence of FRZ, INF and TBOT processes were generally greater in deep soils than shallow soils. During the warm season, the physical processes generally showed more influence on shallow soil temperatures. When it comes to the cold season, the influence of the physical processes on deep layers obviously increased and comparable with that on shallow layers, implying the relatively higher uncertainties of Noah-MP during the cold season.

Most $\Delta\overline{RMSE}$ for SLW are far less than 10%, indicating that all the physical processes have limited influence on the SLW, among which CRS, BTR, and STC showed the smallest effects on SLW (Fig. 6d). The RUN process dominates the performance of SLW simulation, especially at lower layers (70cm and 140cm, Fig. 6d, 5e, and 5f). In addition, the VEG, SFC, FRZ, RAD, and TBOT processes generally showed more influence on deep layers, particularly in the cold season.

3.2.2 Sensitivities of physical processes and general behaviors of parameterizations

To further investigate the sensitivity of each process and the general performance of the parameterizations, the Independent-sample T-test (2-tailed) and Tukey's test were conducted to test whether the difference between parameterizations within a physical process is significant (Fig. 7). In a given sub-process, any two schemes labelled with different letters behave significantly different, and this sub-process therefore can be identified as sensitive. Otherwise, the sub-process is considered insensitive. Moreover, schemes with the letters late in the alphabet have smaller mean RMSEs and outperform the ones with the letters forward in the alphabet. Using the three schemes in vegetation model process (hereafter VEG(1), VEG(3) and VEG(4)) in Fig. 7 as an example. At the depth of 70cm, VEG(3) was labeled with letter "B", while VEG(1) and VEG (4) was labeled with letter "A". For other layers, VEG(1), VEG(3) and VEG(4) were labeled with the letter "A", "C" and "B", respectively. As described above, the VEG process was sensitive for ST simulation. Moreover, VEG(3) had advantages in producing good simulations than VEG(1) and VEG(4) at 70cm depth, and the performance decreased in the order of VEG(3) > VEG(4) > VEG(1) at other layers. In terms of the whole soil column, VEG(3) outperformed VEG(1) and VEG(4).

Consistent with the result in Fig. 6, all other physical processes showed sensitivities in varying magnitudes except the BTR and CRS process. And the performance difference between schemes of the RUN and SFC were obviously greater than other processes. For the RUN process, the performance orders for both ST and SLW simulation generally followed RUN(4) > RUN(1) > RUN(3) > RUN(2) as a whole. For the whole year, RUN(1), RUN(3), and RUN(4) had significant but slightly difference between each other, among which RUN(1) and RUN(4) presented similar performance during both warm and cold seasons (Fig. S2, S3, S4 and S5). During the warm season, the performance of RUN(3) for ST simulation showed notable improvements at shallow layers (5cm and 25cm, Fig. S2). By contrast, RUN(2) performed the worst among the four schemes in spite of the good performance at shallow layers during the cold season (5cm and 25cm in Fig. S3, 25cm in Fig. S5). During both warm and cold seasons, the performance orders for ST simulations were SFC(2) > SFC(1) for SFC process, FRZ(2) > FRZ(1) for FRZ process, and RAD(3) > RAD(1) > RAD(2) for RAD process (Fig. S2 and S3), which are particularly so for SLW simulations at shallow and deep layers. In particular, the FRZ process showed higher sensitivity at the deep soils and during the cold season (Fig. 6, 7 and 8). For the ST simulation, INF(2) performed better at the shallow soils (5cm and 25cm) while did worse at the deep soils compared with INF(1). Despite the slightly good performance of TBOT(2) for ST simulation at the first five layers, TBOT(1) greatly outperformed TBOT(2) at the depth of 300cm. For the STC process, STC(2) greatly excel STC(1) in simulating ST while showed small different with STC(1) when simulating SLW. However, the impact of STC process on SLW increase in line with that on ST during the cold season (Fig. 6).

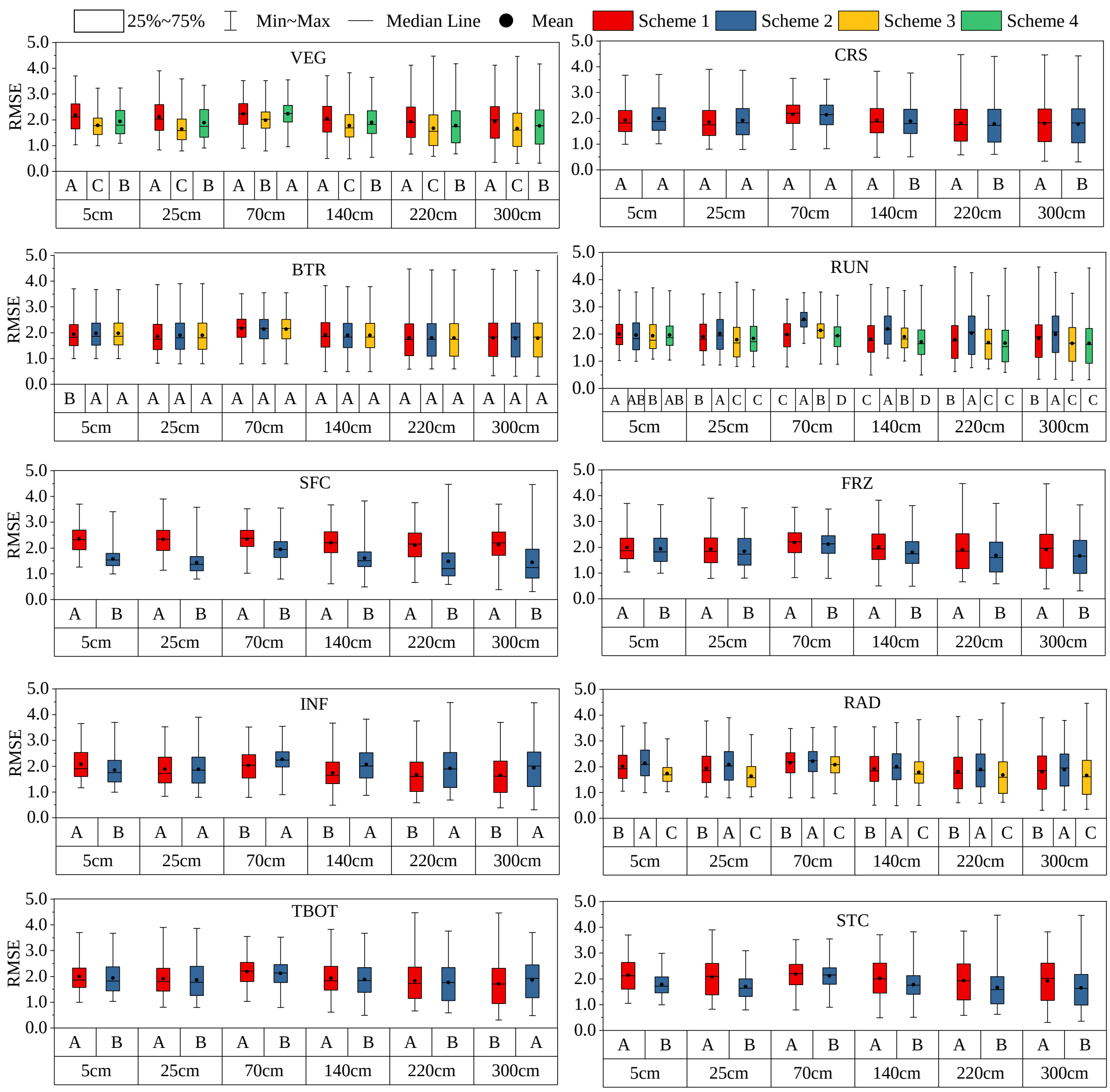

Figure 7. Distinction level for RMSE of ST at different layers during the whole year in the ensemble simulations. Limits of the boxes represent upper and lower quartiles, whiskers extend to the maximum and minimum RMSE. The black stations in the box are the average values. The lines in the box indicate the median value.

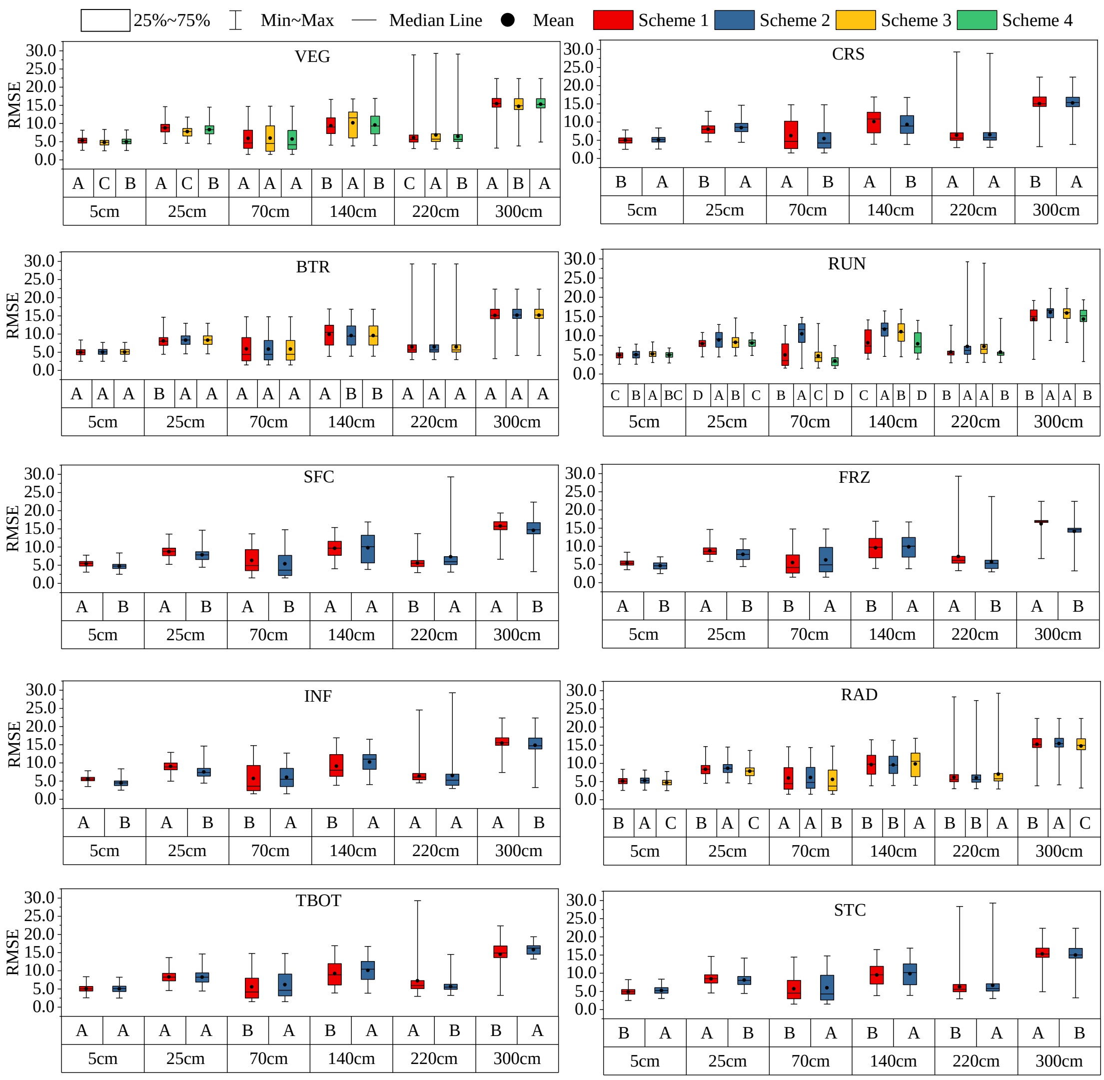

Figure 8. Same as in Figure 7 but for SLW.

3.3 The optimal combination

The CF was calculated to extract the optimal combination of parameterization schemes for ST simulation (Fig. 9). The CF between any two schemes from the same physical process was zero as expected. The CF of RUN(2) and RUN(3) with other schemes was nearly zero, implying that using RUN(2) and RUN (3) provides an extreme less chance of producing favorable simulations than using RUN(1) RUN(4). A higher CF signify greater probability of producing advantageous simulations. For instance, the CF between SFC(2) and VEG(3) was 0.46, about two times than the CFs between SFC(2) and VEG(1)/VEG(4). It indicates that 46% of the 346 best combinations adopted SFC(2) and VEG(3) simultaneously, and the combination of

SFC(2) and VEG(3) tend to induce better ST in comparison of the combination of SFC(2) and VEG(1)/VEG(4).

SFC(2) is firstly determined as one of the schemes that make up the optimal combination, because it was most widely linked to other parameterization schemes with relatively large CFs. Other optimal schemes of each physical process can be determined by choosing the one that has large CF with SFC(2). Obviously, VEG(3), RUN(4), FRZ(2) and INF(1) outperform other schemes in the corresponding physical processes and were selected for optimal combination. The schemes within CRS, BTR, RAD and STC processes scored nearly identical CFs with SFC(2). Due to the insensitivity of CRS and BTR, CRS(1) and BTR(1), which are the default schemes in Noah-MP, were determined as the member schemes of the optimal combination. Combining the selected schemes above with different schemes of RAD and STC processes, there are 6 candidate combinations, among which the one with smallest colRMSE is selected as the optimal combination. Ultimately, the determined schemes for optimal combination is VEG(3), CRS(1), BTR(1), RUN(4), SFC(2), FRZ(2), INF(1), RAD(2), TBOT(2) and STC(1) (Table 1).

The simulated results of the optimal scheme combination well captured the variation of ST (Fig. 4). Despite the overestimation of ST at the shallow soil layers from April to July, the optimal combination well produced the ST during the cold season and of the deep layers (Fig. 4), which is crucial for modeling permafrost features such as active layer thickness and temperature at the top of the permafrost.

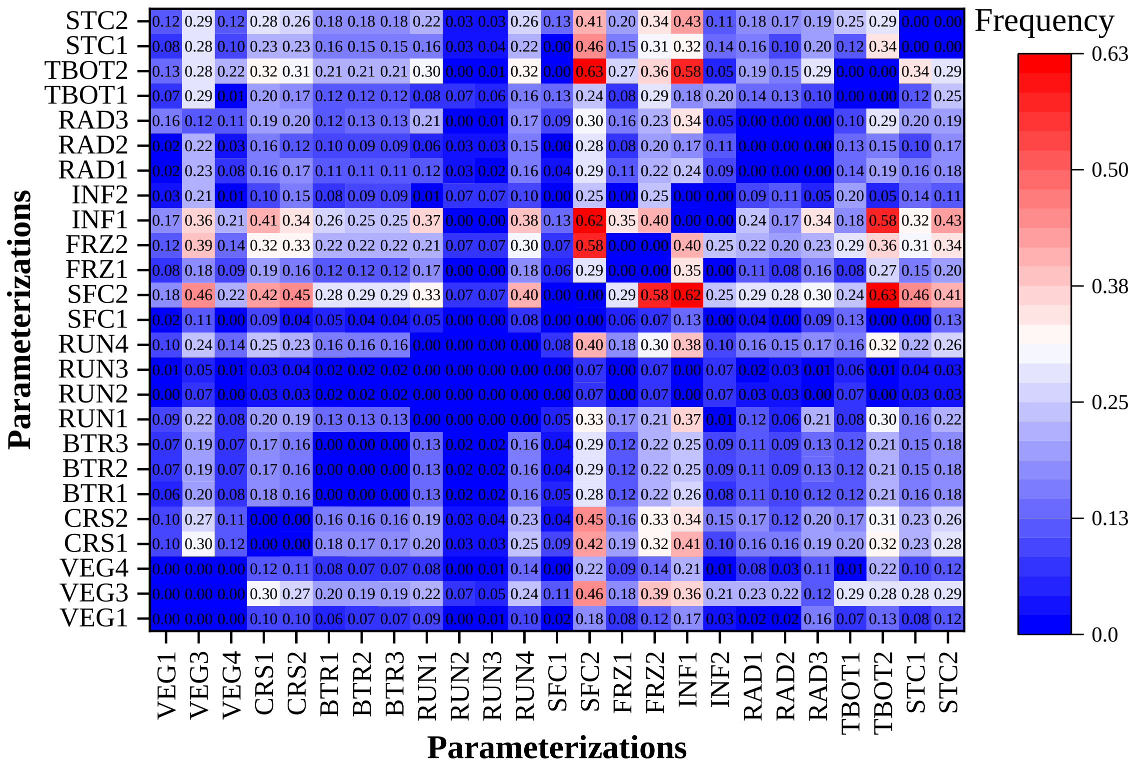

Figure 9. Connection frequency of parameterization schemes.

4 Discussion

4.1 Influence of snow cover on permafrost in the QTP

Reproducing the snow processes remains a persistent challenge for LSMs in the QTP, most of which overestimate the snow depth (Wei and Dong, 2015), including the Noah-MP model (Jiang et al., 2020; Li et al., 2020; Wang et al., 2020). Our ensemble simulations also show that the surface albedo is extremely overestimated in both magnitude and duration (Fig. 2), implying an extreme overestimation of snow cover. The overestimation is ascribed to many causes, such as the vegetation effect (Park et al., 2016), the snow cover fraction (Jiang et al., 2020), the sublimation from wind (Yuan et al., 2016; Li et al., 2020), and the fresh snow albedo (Wang et al. 2020). More need to be done in the future to quantify the influence of these physics.

However, snow cover in the permafrost regions of the QTP is thin, patchy, and short-lived (Che et al., 2019) because of the high wind speed (Yuan et al., 2016; Xie et al., 2019) and strong solar radiation (Meng et al., 2018). Its influence on soil temperature and contribution to permafrost state is usually considered weak (Jin et al., 2008). The in-situ measurements at TGL site also showed limited influence on soil temperature (Fig. 3), which is consistent with the studies at an alpine wetland site (Zhang et al., 2018) and the Yellow River source (Yao et al., 2019) on the QTP. The insufficient of numerical models for snow simulation seriously suppresses the accuracy of soil temperature (Fig. S1). For practical purpose, the snow processes is usually neglected when modeling the permafrost state in the QTP (Qin et al., 2017; Zou et al., 2017; Wu et al., 2018).

4.2 Possible reasons for the cold bias of soil temperature

The cold bias of soil temperature on the QTP are widely reported in many of the state-of-the-art LSMs (Yang et al., 2009;Chen et al., 2019). One of the main reason can be the inability of representing the diurnal variation of roughness length for heat (Z_{0h}) on the QTP (Yang et al., 2008; Chen et al., 2010), which is of great importance for a reliable calculation of the sensible and latent heat, and thus for the soil surface/profile temperature calculation (Zeng et al., 2012; Zheng et al., 2012). Noah-MP parameterize Z_{0h} in the two schemes of SFC process (Table 1). In the M-O scheme, Z_{0h} is taken as the same with the roughness length for momentum (Z_{0m}, Niu et al., 2011). The Chen97 scheme adopts the Zilitinkevitch approach (Zilitinkevich, 1995). However, both of them couldn't produce the diurnal variation of $Z_{0,h}$ (Chen et al., 2010).

Another possible reason is the poor representation of the thermal conductivity (λ) of frozen soil. Considering that the λ of ice is nearly four times higher than liquid water, λ of frozen soil is generally expected to be greater than that of unfrozen soil. Many parameterization schemes of λ, including the Johansen scheme in Noah-MP, follow this pattern (Du et al., 2020). However, contrary phenomenon is widely reported over the QTP (Pan et al., 2016; Hu et al., 2017; Yi et al., 2018; Li et al., 2019), including the TGL site (Li et al., 2019). As a result, a majority of the state-of-the-art LSMs have tended to overestimate the soil thermal conductivity of the QTP (Luo et al., 2009; Chen et al., 2012; Du et al., 2020), which exactly explains the underestimation of soil temperature during cold season and, at times, an overestimation during the warm season (Luo et al., 2009).

4.3 Discussions on the sensitivity of physical processes

4.3.1 Vegetation model (VEG) and canopy gap for radiation transfer (RAD)

Noah-MP computes energy fluxes in vegetated fraction and bare fraction separately and then sum them up weighted by vegetation fraction (FVEG). As list in Table 1, VEG process includes three options to calculate FVEG in this study. VEG(3) calculates the daily FVEG based on the interpolated LAI, while VEG(1) and VEG(4) uses the prescribed monthly and maximum FVEG, respectively. Obviously, VEG(3) produces more realistic FVEG over the year, followed by VEG(1) and VEG(4). VEG(4) grossly overestimates the FVEG, especially that during the cold season. Consequently, VEG(3) outperformed VEG(1) and VEG(4). However, VEG(4) is widely used in many studies (Gao et al., 2015; Chen et al., 2016; Li et al., 2018) despite overestimating the FVEG. In this study, VEG(4) performed better than VEG(1).

RAD treats the radiation transfer process within the vegetation, and adopts three methods to calculate the canopy gap. RAD(1) defines canopy gap as a function of the 3D vegetation structure and the solar zenith angle, RAD(2) employs no gap within canopy, and RAD(3) treat the canopy gap from unity minus the FVEG (Niu and Yang, 2004). The RAD(3) scheme penetrates the most solar radiation to the ground, followed by the RAD(1) and RAD(2) schemes. As an alpine grassland, there is a relative low LAI at TGL site, and thus a quite high canopy gap. So, schemes with a larger canopy gap could realistically reflect the environment. Consequently, the performance decreased in the order of RAD(3) > RAD(1) > RAD(2) for ST/SLW simulation.

4.3.2 Canopy stomatal resistance (CRS) and soil moisture factor for stomatal resistance (BTR)

The biophysical process BTR and CRS directly affect the canopy stomatal resistance and thus the plant transpiration (Niu et al., 2011). The transpiration of plants could impact the ST through its cooling effect (Shen et al., 2015) and the water balance of root zone (Chang et al., 2020). However, the annual transpiration of alpine steppe is weak due to the shallow effective root zone and lower stomatal control in this dry environment (Ma et al., 2015), which may explain the indistinctive or very small difference among the schemes of the BTR and CRS processes (Fig. 7 and 8).

4.3.3 Runoff and groundwater (RUN)

For the RUN process, RUN(2) had the worst performance for simulating ST and SLW (Fig. 7 and 8) among the four schemes, likely due to its higher estimation of soil moisture (Fig. S6) and thus greater sensible heat and smaller ST (Gao et al., 2015). Consistent with the study of Li et al. (2015), RUN(3) performed the best at shallow layers for ST during the warm season, while that for SLW were less good. However, RUN(4) outperformed RUN(3) at deep layers, which may be explained by the better agreement of SLW by RUN(4) (Fig. 8 and S6).Likewise, RUN(4) was on a par with RUN(1) in the simulation of ST due to the very small difference in SLW of two schemes (Fig. 8 and S6). For the whole soil column, RUN(4) surpassed RUN(1) and RUN(2), both of which define surface/subsurface runoff as functions of groundwater table depth (Niu et al., 2005; Niu et al., 2007). This is in keeping with the study of Zheng et al. (2017) that soil water storage-based parameterizations outperform the groundwater table-based parameterizations in simulating the total runoff in a seasonally frozen and high-altitude Tibetan river, Besides, RUN(4) is designed based on the infiltration-excess runoff (Yang and Dickinson, 1996) in spite of the saturation-excess runoff in RUN(1) and RUN(2) (Gan et al., 2019), which is more common in arid and semiarid areas like the permafrost regions of QTP (Pilgrim et al., 1988).

4.3.4 Surface layer drag coefficient (SFC)

SFC defines the calculations of the surface exchange coefficient for heat and water vapor (CH), which greatly impact the energy and water balance and thus the temperature and moisture of soil. SFC(1) adopts the Monin-Obukhov similarity theory (MOST) with a general form, while the SFC(2) uses the improved MOST modified by

Chen et al. (1997). The most distinct difference between them is that SFC(1) considers the zero-displacement height while SFC(2) parameterizes Z_{0h} and Z_{0m} using different schemes. The difference between SFC(1) and SFC(2) has a great impact on the CH value. Several studies have reported that SFC(2) has a better performance for the simulation of sensible and latent heat on the QTP (Zhang et al., 2016; Gan et al., 2019). The results of T-test in this study showed remarkable distinctions between the two schemes, where SFC(2) was dramatically superior to SFC(1) (Fig. 7 and 8). SFC(2) produces lower CH than SFC(1) (Zhang et al., 2014), resulting in less efficient ventilation and greater heating of the land surface (Yang et al., 2011b), and substantial improvement of the cold bias of Noah-MP in this study (Fig. 4). As the sensible heat rising, the latent heat decline (Gao et al., 2015) and the dry bias of Noah-MP is mitigated (Fig. 8).

4.3.5 Super-cooled liquid water (FRZ) and frozen soil permeability (INF)

FRZ treats liquid water in frozen soil (super-cooled liquid water) using two forms of freezing-point depression equation. FRZ(1) takes a general form (Niu and Yang, 2006), while FRZ(2) exhibits a variant form that considers the increased surface area of icy soil particles (Koren et al., 1999). FRZ(2) generally yields more liquid water in comparison of FRZ(1). For ST simulation, FRZ process did not show sensitivity at the shallow soil layers (5cm and 25cm) during the warm season (Fig. S2), but showed an increasing sensitivity at the deep layers, especially during the cold season (Fig. 4 and S3). This can be related to the greater sensitivity of FRZ (Fig. 4, S4 and S5) and the longer frozen duration at deep soil and during the cold season.

INF(1) uses soil moisture (Niu and Yang, 2006) while INF(2) employs only the liquid water (Koren et al., 1999) to parameterize soil hydraulic properties. INF(2) generally produces more impermeable frozen soil than INF(1), which is also found in this study (Fig. S7). Due to the more realistic representation of SLW during the cold season (Fig. S7), INF(2) surpassed INF(1) in simulating ST at 5 cm depth, while INF(1) outperformed INF(2) at 70 cm, 140 cm and 220 cm (Fig. 7). This result also indicate that INF(1) and INF(2) could alleviate the overestimation and underestimation of SLW, respectively. INF(2) simulated worse ST than INF(1) at 300 cm depth (Fig. 7) in spite of the better agreement with observed SLW (Fig. 8 and S7), which may be related to the overestimation of soil moisture of INF(2) at the depth of 140 cm.

4.3.6 Lower boundary of soil temperature (TBOT) and snow/soil temperature time scheme (STC)

TBOT process adopts two schemes to describe the soil temperature boundary conditions. TBOT (1) assumes zero heat flux at the bottom of the model, while TBOT(2) adopts the soil temperature at the 8 m depth (Yang et al., 2011a). In general, TBOT(1) is expected to accumulate heat in the deep soil and produce higher ST than TBOT(2). In this study, the two assumptions performed significantly different, especially at the deep soil. Although TBOT(2) is more representative of the realistic condition, TBOT(1) greatly surpassed TBOT(2) at the depth of 300cm. It can be related to the overall underestimation of the model, which can be alleviated by TBOT(1) because of heat accumulation (Fig. S8).

Two time discretization strategies are implemented in the STC process, where STC(1) adopts the semi-implicit scheme while STC(2) uses the full implicit scheme, to solve the thermal diffusion equation in first soil or snow layers (Yang et al., 2011a). STC(1) and STC(2) are not strictly a physical processes but different upper boundary conditions of soil column (You et al., 2019). The differences between STC(1) and STC(2) were significant (Fig. 7). Snow processes are not involved in this study, the impacts of the two options on ST is remarkable (Fig. 6), particularly in the shallow layers and during the cold season (Fig. 6). In addition, STC(2) outperformed STC(1) in the ensemble simulated ST(Fig. 7), because the higher ST produced by STC(2) (Fig. S9) alleviated the overall underestimation of Noah-MP.

4.4 Perspectives

This study analyzed the characteristics and general behaviors of each parameterization scheme of Noah-MP at a typical permafrost site on the QTP, hoping to provide a reference for simulating permafrost state on the QTP. We identified the systematic overestimation of snow cover and cold bias in Noah-MP, and discussed the possible sources of error. Relevant results and methodologies can be practical guidelines for improving the parameterizations of physical processes and testing their uncertainties towards near-surface permafrost modeling on the plateau. Although the site we selected may be representative for the typical environment on the plateau, continued investigation with a broad spectrum of climate and environmental conditions is required to make a general conclusion at regional scale.

5 Conclusions

In this study, an ensemble simulation using multi-parameterizations was conducted using the Noah-MP model at the TGL site, aiming to provide a reference for permafrost simulation using LSMs. The model was modified to consider the vertical heterogeneity in the soil and the simulation depth was extended to cover the whole active layer. The ensemble simulation consists of 6912 parameterization experiments, combining ten physical processes (VEG, CRS, BTR, RUN, SFC, FRZ, INF, RAD, TBOT, and STC) each with multiple optional schemes. On this basis, the general performance of Noah-MP was assessed by comparing simulation results with in situ observations, and the sensitivity of soil temperature and moisture at different depth of active layer to parameterization schemes was explored. Furthermore, we proposed a new method to extract the optimal combination of schemes to simulate soil temperature in the permafrost regions of the QTP. The main conclusions are as follows:

(1) Noah-MP model tends to overestimate snow cover and thus largely underestimate soil temperature in the permafrost regions of the QTP. Systematic cold bias and large uncertainties of soil temperature still exist after removing the snow processes, particularly at the deep layers and during the cold season. This is largely due to the imperfect model structure with regard to the roughness length for heat and soil thermal conductivity.

(2) Soil temperature is dominated by the surface layer drag coefficient (SFC) while

largely influenced by runoff and groundwater (RUN). Other physical processes have little impact on ST simulation, among which VEG, RAD, and STC are more influential on shallow ST, while FRZ, INF and TBOT have greater impacts on deep ST. In addition, CRS and BTR do not significantly affect the simulation results.

(3) The best scheme combination for permafrost simulation are as follows: VEG (table LAI, calculated vegetation fraction), CRS (Jarvis), BTR (Noah), RUN (BATS), SFC (Chen97), RAD (zero canopy gap), FRZ (variant freezing-point depression), INF (hydraulic parameters defined by soil moisture), TBOT (ST at 8 m), STC (semi-implicit).

Code availability. The source code of offline 1D Noah-MP LSM v1.1 is available at https://ral.ucar.edu/solutions/products/noah-multiparameterization-land-surface-model-noah-mp-lsm (last access: 15 May 2020). The modified Noah-MP with the consideration of vertical heterogeneity, extended soil depth, and pedotransfer functions is available upon request to the corresponding author. The data processing code are available at http://dx.doi.org/10.17632/gc7vfgkyng.1.

Data availability. The 1-hourly forcing data and daily soil temperature data at the TGL site are available at http://dx.doi.org/10.17632/gc7vfgkyng.1. Soil texture data can be obtained at https://doi.org/10.1016/j.catena.2017.04.011 (Hu et al., 2017). The AVHRR LAI data can be downloaded from https://www.ncei.noaa.gov/data/ (Claverie et al., 2016).

Author contributions. TW and XL conceived the idea and designed the model experiments. XL performed the simulations, analyzed the output, and wrote the paper. XW, XZ, GH, RL contributed to the conduction of the simulation and interpretation of the results. YQ provided the observations of atmospheric forcing and soil temperature. CY and JH helped in downloading and processing the AVHRR LAI data. JN and WM provide guidelines for the visualization. Everyone revised and polished the paper.

Competing interests. The authors declare that they have no conflict of interest.

Acknowledgements. This work has been supported by the CAS "Light of West China" Program, and the National Natural Science Foundation of China (41690142; 41771076; 41961144021; 41671070). The authors thank Cryosphere Research Station on the Qinghai-Tibet Plateau, CAS for providing field observation data used in this study. We would like to thank two anonymous reviewers for their insightful and constructive comments and suggestions, which greatly improved the quality of the manuscript.

References

Benjamini, Y.: Simultaneous and selective inference: Current successes and future challenges, Biometrical J., 52, 708-721, https://doi.org/10.1002/bimj.200900299, 2010.

Cao, B., Zhang, T., Wu, Q., Sheng, Y., Zhao, L., and Zou, D.: Brief communication: Evaluation and inter-comparisons of Qinghai–Tibet Plateau permafrost maps based on a new inventory of field evidence, The Cryosphere, 13, 511-519, https://doi.org/10.5194/tc-13-511-2019, 2019.

Chang, M., Liao, W., Wang, X., Zhang, Q., Chen, W., Wu, Z., and Hu, Z.: An optimal ensemble of the Noah-MP land surface model for simulating surface heat fluxes over a typical subtropical forest in South China, Agric. For. Meteor., 281, 107815, https://doi.org/https://doi.org/10.1016/j.agrformet.2019.107815, 2020.

Che, T., Hao, X., Dai, L., Li, H., Huang, X., and Xiao, L.: Snow cover variation and its impacts over the Qinghai-Tibet Plateau, Bull. Chin. Acad. Sci., 34, 1247-1253, https://doi.org/10.16418/j.issn.1000-3045.2019.11.007, 2019.

Chen, F., Janjić, Z., and Mitchell, K.: Impact of atmospheric surface-layer parameterizations in the new land-surface scheme of the NCEP Mesoscale Eta Model. Boundary-Layer Meteorol. 85, 391-421, https://doi.org/10.1023/A:1000531001463, 1997.

Chen, L., Li, Y., Chen, F., Barr, A., Barlage, M., and Wan, B.: The incorporation of an organic soil layer in the Noah-MP land surface model and its evaluation over a boreal aspen forest, Atmos. Chem. Phys., 16, 8375-8387, https://doi.org/10.5194/acp-16-8375-2016, 2016.

Chen, R., Yang, M., Wang, X., and Wan, G.: Review on simulation of land-surface processes on the Tibetan Plateau, Sci. Cold Arid Reg., 11, 93-115, https://doi.org/10.3724/SP.J.1226.2019.00093, 2019.

Chen, S., Li, X., Wu, T., Xue, K., Luo, D., Wang, X., Wu, Q., Kang, S., Zhou, H., and Wei, D.: Soil thermal regime alteration under experimental warming in permafrost regions of the central Tibetan Plateau, Geoderma, 372, 114397, https://doi.org/https://doi.org/10.1016/j.geoderma.2020.114397, 2020.

Chen, Y., Yang, K., Zhou, D., Qin, J., and Guo, X.: Improving the Noah Land Surface Model in Arid Regions with an Appropriate Parameterization of the Thermal Roughness Length, J.

Hydrometeor., 11, 995-1006, https://doi.org/10.1175/2010JHM1185.1, 2010.
Chen, Y., Yang, K., Tang, W., Qin, J., and Zhao, L.: Parameterizing soil organic carbon's impacts on soil porosity and thermal parameters for Eastern Tibet grasslands, Sci. Chin. Earth Sci., 55, 1001-1011, https://doi.org/10.1007/s11430-012-4433-0, 2012.
Claverie, M., Matthews, J. L., Vermote, E. F., and Justice, C. O.: A 30+ Year AVHRR LAI and FAPAR Climate Data Record: Algorithm Description and Validation, Remote Sens., 8, 263, https://doi.org/10.3390/rs8030263, 2016.
Cosby, B. J., Hornberger, G. M., Clapp, R. B., and Ginn, T. R.: A Statistical Exploration of the Relationships of Soil Moisture Characteristics to the Physical Properties of Soils, Water Resour. Res., 20, 682-690, https://doi.org/10.1029/WR020i006p00682, 1984.
Daniel, R., Nikolay, S., Bernd, E., Stephan, G., and Sergei, M.: Recent advances in permafrost modelling, Permafr. Periglac. Process., 19, 137-156, https://doi.org/doi:10.1002/ppp.615, 2008.
Du, Y., Li, R., Zhao, L., Yang, C., Wu, T., Hu, G., Xiao, Y., Zhu, X., Yang, S., Ni, J., and Ma, J.: Evaluation of 11 soil thermal conductivity schemes for the permafrost region of the central Qinghai-Tibet Plateau, CATENA, 193, 104608, https://doi.org/https://doi.org/10.1016/j.catena.2020.104608, 2020.
Fountain, A. G., Campbell, J. L., Schuur, E. A. G., Stammerjohn, S. E., Williams, M. W., and Ducklow, H. W.: The Disappearing Cryosphere: Impacts and Ecosystem Responses to Rapid Cryosphere Loss, BioScience, 62, 405-415, https://doi.org/10.1525/bio.2012.62.4.11, 2012.
Gan, Y. J., Liang, X. Z., Duan, Q. Y., Chen, F., Li, J. D., and Zhang, Y.: Assessment and Reduction of the Physical Parameterization Uncertainty for Noah-MP Land Surface Model, Water Resour. Res., 55, 5518-5538, https://doi.org/10.1029/2019wr024814, 2019.
Gao, Y., Kai, L., Fei, C., Jiang, Y., and Lu, C.: Assessing and improving Noah-MP land model simulations for the central Tibetan Plateau, J. Geophys. Res.-Atmos., 120, 9258-9278, 2015.
Guo, D., and Wang, H.: Simulation of permafrost and seasonally frozen ground conditions on the Tibetan Plateau, 1981-2010, J. Geophys. Res.-Atmos., 118, 5216-5230, https://doi.org/10.1002/jgrd.50457, 2013.
He, K., Sun, J., and Chen, Q.: Response of climate and soil texture to net primary productivity and precipitation-use efficiency in the Tibetan Plateau, Pratacultural Science, 36, 1053–1065. https://doi.org/10.11829/j.issn.1001-0629.2019-0036, 2019.
Hillel, D.: Applications of Soil Physics, Academic Press, 400 pp., 1980.
Hjort, J., Karjalainen, O., Aalto, J., Westermann, S., Romanovsky, V. E., Nelson, F. E., Etzelmüller, B., and Luoto, M.: Degrading permafrost puts Arctic infrastructure at risk by mid-century, Nat. Commun., 9, 5147, https://doi.org/10.1038/s41467-018-07557-4, 2018.
Hong, S., Yu, X., Park, S. K., Choi, Y. S., and Myoung, B.: Assessing optimal set of implemented physical parameterization schemes in a multi-physics land surface model using genetic algorithm, Geosci. Model Dev., 7, 2517-2529, https://doi.org/10.5194/gmd-7-2517-2014, 2014.
Hu, G., Zhao, L., Li, R., Wu, T., Wu, X., Pang, Q., Xiao, Y., Qiao, Y., and Shi, J.: Modeling hydrothermal transfer processes in permafrost regions of Qinghai-Tibet Plateau in China, Chin. Geograph. Sci., 25, 713-727, https://doi.org/10.1007/s11769-015-0733-6, 2015.
Hu, G., Zhao, L., Wu, X., Li, R., Wu, T., Xie, C., Pang, Q., and Zou, D.: Comparison of the thermal conductivity parameterizations for a freeze-thaw algorithm with a multi-layered soil in permafrost regions, Catena, 156, 244-251, https://doi.org/10.1016/j.catena.2017.04.011, 2017.
Jiang, Y., Chen, F., Gao, Y., He, C., Barlage, M., and Huang, W.: Assessment of uncertainty sources

in snow cover simulation in the Tibetan Plateau, J. Geophys. Res.-Atmos., 125, e2020JD032674, https://doi.org/10.1029/2020JD032674, 2020.

Jin, H., Sun, L., Wang, S., He, R., Lu, L., and Yu, S.: Dual influences of local environmentalVariables on ground temperatures on the interior-eastern Qinghai-Tibet Plateau (I): vegetation and snow cover. J. Glaciol. Geocryol. 30, 535–545, 2008.

Koren, V., Schaake, J., Mitchell, K., Duan, Q. Y., Chen, F., and Baker, J. M.: A parameterization of snowpack and frozen ground intended for NCEP weather and climate models, J. Geophys. Res.-Atmos., 104, 19569-19585, https://doi.org/10.1029/1999JD900232, 1999.

Koven, C., Riley, W., and Stern, A.: Analysis of Permafrost Thermal Dynamics and Response to Climate Change in the CMIP5 Earth System Models, J. Clim., 26, 1877-1900, https://doi.org/10.1175/JCLI-D-12-00228.1, 2013.

Lawrence, D., Fisher, R., Koven, C., Oleson, K., Swenson, S., Vertenstein, M.: Technical description of version 5.0 of the Community Land Model (CLM), Boulder, Colorado, 2018.

Li, J., Chen, F., Zhang, G., Barlage, M., Gan, Y., Xin, Y., and Wang, C.: Impacts of Land Cover and Soil Texture Uncertainty on Land Model Simulations Over the Central Tibetan Plateau, J. Adv. Model. Earth Sy., 10, 2121-2146, https://doi.org/10.1029/2018ms001377, 2018.

Li, K., Gao, Y., Fei, C., Xu, J., Jiang, Y., Xiao, L., Li, R., and Pan, Y.: Simulation of impact of roots on soil moisture and surface fluxes over central Qinghai − Xizang Plateau. Plateau Meteor., 34, 642-652, https://doi.org/10.7522/j.issn.1000-0534.2015.00035, 2015.

Li, R., Zhao, L., Wu, T., Wang, Q. X., Ding, Y., Yao, J., Wu, X., Hu, G., Xiao, Y., Du, Y., Zhu, X., Qin, Y., Shuhua, Y., Bai, R., Erji, D., Liu, G., Zou, D., Yongping, Q., and Shi, J.: Soil thermal conductivity and its influencing factors at the Tanggula permafrost region on the Qinghai–Tibet Plateau, Agric. For. Meteor., 264, 235-246, https://doi.org/10.1016/j.agrformet.2018.10.011, 2019.

Li, X., Wu, T., Zhu, X., Jiang, Y., Hu, G., Hao, J., Ni, J., Li, R., Qiao, Y., Yang, C., Ma, W., Wen, A., and Ying, X.: Improving the Noah-MP Model for simulating hydrothermal regime of the active layer in the permafrost regions of the Qinghai-Tibet Plateau, J. Geophys. Res.-Atmos., 125, e2020JD032588, https://doi.org/10.1029/2020JD032588, 2020.

Luo, D., Wu, Q., Jin, H., Marchenko, S., Lyu, L., and Gao, S.: Recent changes in the active layer thickness across the northern hemisphere, Environ. Earth Sci., 75, 555. https://doi.org/10.1007/s12665-015-5229-2, 2016.

Luo, S., Lyu, S., Zhang, Y., Hu, Z., Ma, Y. M., Li, S. S., and Shang, L.: Soil thermal conductivity parameterization establishment and application in numerical model of central Tibetan Plateau, Chin. J. Geophys., 52, 919-928, https://doi.org/10.3969/j.issn.0001-5733.2009.04.008, 2009.

Ma, N., Zhang, Y., Guo, Y., Gao, H., Zhang, H., and Wang, Y.: Environmental and biophysical controls on the evapotranspiration over the highest alpine steppe, J. Hydrol., 529, 980-992, https://doi.org/https://doi.org/10.1016/j.jhydrol.2015.09.013, 2015.

Maheu, A., Anctil, F., Gaborit, É., Fortin, V., Nadeau, D. F., and Therrien, R.: A field evaluation of soil moisture modelling with the Soil, Vegetation, and Snow (SVS) land surface model using evapotranspiration observations as forcing data, J. Hydrol., 558, 532-545, https://doi.org/https://doi.org/10.1016/j.jhydrol.2018.01.065, 2018.

Melton, J., Verseghy, D., Sospedra-Alfonso, R., and Gruber, S.: Improving permafrost physics in the coupled Canadian Land Surface Scheme (v.3.6.2) and Canadian Terrestrial Ecosystem Model (v.2.1) (CLASS-CTEM), Geosci. Model Dev., 12, 4443-4467, https://doi.org/10.5194/gmd-12-

4443-2019, 2019.

Nicolsky, D. J., Romanovsky, V. E., Alexeev, V. A., and Lawrence, D. M.: Improved modeling of permafrost dynamics in a GCM land-surface scheme, Geophys. Res. Lett., 34, L08501, https://doi.org/10.1029/2007gl029525, 2007.

Niu, G.-Y., and Yang, Z.-L.: Effects of vegetation canopy processes on snow surface energy and mass balances, J. Geophys. Res.-Atmos., 109, D23111, https://doi.org/10.1029/2004jd004884, 2004.

Niu, G.-Y., and Yang, Z.-L.: Effects of Frozen Soil on Snowmelt Runoff and Soil Water Storage at a Continental Scale, J. Hydrometeor., 7, 937-952, https://doi.org/10.1175/JHM538.1, 2006.

Niu, G.-Y., Yang, Z.-L., Dickinson, R. E., and Gulden, L. E.: A simple TOPMODEL-based runoff parameterization (SIMTOP) for use in global climate models, J. Geophys. Res.-Atmos., 110, D21106, https://doi.org/10.1029/2005jd006111, 2005.

Niu, G.-Y., Yang, Z.-L., Dickinson, R. E., Gulden, L. E., and Su, H.: Development of a simple groundwater model for use in climate models and evaluation with Gravity Recovery and Climate Experiment data, J. Geophys. Res.-Atmos., 112, D07103, https://doi.org/10.1029/2006jd007522, 2007.

Niu, G.-Y., Yang, Z.-L., Mitchell, K. E., Chen, F., Ek, M. B., Barlage, M., Kumar, A., Manning, K., Niyogi, D., and Rosero, E.: The community Noah land surface model with multiparameterization options (Noah-MP): 1. Model description and evaluation with local-scale measurements, J. Geophys. Res.-Atmos., 116, D12109, https://doi.org/10.1029/2010JD015139, 2011.

Pan, X., Li, Y., Yu, Q., Shi, X., Yang, D., and Roth, K.: Effects of stratified active layers on high-altitude permafrost warming: a case study on the Qinghai–Tibet Plateau, The Cryosphere, 10, 1591-1603, https://doi.org/10.5194/tc-10-1591-2016, 2016.

Park, S., and Park, S.K.: Parameterization of the snow-covered surface albedo in the Noah-MP Version 1.0 by implementing vegetation effects, Geosci. Model Dev. 9, 1073-1085, https://doi.org/10.5194/gmd-9-1073-2016, 2016.

Pilgrim, D. H., Chapman, T. G., and Doran, D. G.: Problems of rainfall-runoff modelling in arid and semiarid regions, Hydrolog. Sci. J., 33, 379-400, https://doi.org/10.1080/02626668809491261, 1988.

Qin, Y., Wu, T., Zhao, L., Wu, X., Li, R., Xie, C., Pang, Q., Hu, G., Qiao, Y., Zhao, G., Liu, G., Zhu, X., and Hao, J.: Numerical modeling of the active layer thickness and permafrost thermal state across Qinghai-Tibetan Plateau. J. Geophys. Res.-Atmos., 122, 11,604-611,620, https://doi.org/10.1002/2017JD026858, 2017.

Ran, Y., Xin, L., and Cheng, G.: Climate warming over the past half century has led to thermal degradation of permafrost on the Qinghai–Tibet Plateau, Cryosphere, 12, 595-608, https://doi.org/10.5194/tc-12-595-2018, 2018.

Schaake, J. C., Koren, V. I., Duan, Q. Y., Mitchell, K., and Chen, F.: Simple water balance model for estimating runoff at different spatial and temporal scales, J. Geophys. Res.-Atmos., 101, 7461-7475, https://doi.org/10.1029/95jd02892, 1996.

Shen, M., Piao, S., Jeong, S.-J., Zhou, L., Zeng, Z., Ciais, P., Chen, D., Huang, M., Jin, C.-S., Li, L. Z. X., Li, Y., Myneni, R. B., Yang, K., Zhang, G., Zhang, Y., and Yao, T.: Evaporative cooling over the Tibetan Plateau induced by vegetation growth, Proc. Natl. Acad. Sci. U. S. A., 112, 9299-9304, https://doi.org/10.1073/pnas.1504418112, 2015.

Wang, W., Yang, K., Zhao, L., Zheng, Z., Lu, H., Mamtimin, A., Ding, B., Li, X., Zhao, L., Li, H., Che, T., and Moore, J. C.: Characterizing Surface Albedo of Shallow Fresh Snow and Its Importance for Snow Ablation on the Interior of the Tibetan Plateau, J. Hydrometeor., 21, 815-827, https://doi.org/10.1175/JHM-D-19-0193.1, 2020.

Wei, Z., and Dong, W.: Assessment of Simulations of Snow Depth in the Qinghai-Tibetan Plateau Using CMIP5 Multi-Models, Arct. Antarct. Alp. Res., 47, 611-525, https://doi.org/10.1657/AAAR0014-050, 2015.

Westermann, S., Langer, M., Boike, J., Heikenfeld, M., Peter, M., Etzelmuller, B., and Krinner, G.: Simulating the thermal regime and thaw processes of ice-rich permafrost ground with the land-surface model CryoGrid 3, Geosci. Model Dev., 9, 523-546, https://doi.org/10.5194/gmd-9-523-2016, 2016.

Wetzel, P., and Chang, J.-T.: Concerning the Relationship between Evapotranspiration and Soil Moisture, J. Clim. Appl. Meteorol., 26, 18-27, https://doi.org/10.1175/1520-0450(1987)026<0018:CTRBEA>2.0.CO;2, 1987.

Woo, M. K.: Permafrost Hydrology, Springer, Berlin, Heidelberg, 2012.

Wu, X., and Nan, Z.: A multilayer soil texture dataset for permafrost modeling over Qinghai-Tibetan Plateau. Paper presented at 2016 IEEE International Geoscience and Remote Sensing Symposium (IGARSS), Beijing, China. https://doi.org/10.1109/IGARSS.2016.7730283, 2016.

Wu, X. B., Nan, Z. T., Zhao, S. P., Zhao, L., and Cheng, G. D.: Spatial modeling of permafrost distribution and properties on the Qinghai-Tibet Plateau, Permafr. Periglac. Process., 29, 86-99, https://doi.org/10.1002/ppp.1971, 2018.

Xie, Z., Hu, Z., Ma, Y., Sun, G., Gu, L., Liu, S., Wang, Y., Zheng, H., and Ma, W.: Modeling blowing snow over the Tibetan Plateau with the community land model: Method and preliminary evaluation, J. Geophys. Res.-Atmos., 124, 9332–9355, https://doi.org/10.1029/2019jd030684, 2019.

Yang, K., Koike, T., Ye, B., and Bastidas, L.: Inverse analysis of the role of soil vertical heterogeneity in controlling surface soil state and energy partition, J. Geophys. Res.-Atmos., 110, D08101, https://doi.org/10.1029/2004jd005500, 2005.

Yang, K., Koike, T., Ishikawa, H., Kim, J., Li, X., Liu, H., Shaomin, L., Ma, Y., and Wang, J.: Turbulent Flux Transfer over Bare-Soil Surfaces: Characteristics and Parameterization, J. Appl. Meteorol. Clim., 47, 276-290, https://doi.org/10.1175/2007JAMC1547.1, 2008.

Yang, K., Chen, Y. Y., and Qin, J.: Some practical notes on the land surface modeling in the Tibetan Plateau, Hydrol. Earth Syst. Sci., 13, 687-701, https://doi.org/10.5194/hess-13-687-2009, 2009.

Yang, Z.-L., and Dickinson, R. E.: Description of the biosphere-atmosphere transfer scheme (BATS) for the soil moisture workshop and evaluation of its performance, Global Planet. Change, 13, 117-134, https://doi.org/10.1016/0921-8181(95)00041-0, 1996.

Yang, Z.-L., Cai, X., Zhang, G., Tavakoly, A., Jin, Q., Meyer, L., and Guan, X.: The Community Noah Land Surface Model with Multi-Parameterization Options (Noah-MP): Technical Description, 2011a.

Yang, Z.-L., Niu, G.-Y., E. Mitchell, K., Chen, F., B. Ek, M., Barlage, M., Longuevergne, L., Manning, K., Niyogi, D., Tewari, M., and Xia, Y.: The community Noah land surface model with multiparameterization options (Noah-MP): 2. Evaluation over global river basins. J. Geophys. Res.-Atmos. 116, D12110, https://doi.org/10.1029/2010JD015140, 2011b.

Yao, C., Lyu, S., Wang, T., Wang, J., and Ma, C.: Analysis on freezing-thawing characteristics of soil in high and low snowfall years in source region of the Yellow River, Plateau Meteor., 38, 474-483, 2019.

Yao, J., Zhao, L., Gu, L., Qiao, Y., and Jiao, K.: The surface energy budget in the permafrost region of the Tibetan Plateau, Atmos. Res., 102, 394-407, https://doi.org/https://doi.org/10.1016/j.atmosres.2011.09.001, 2011.

Yi, S., Zhou, Z., Ren, S., Ming, X., Yu, Q., Shengyun, C., and Baisheng, Y.: Effects of permafrost degradation on alpine grassland in a semi-arid basin on the Qinghai–Tibetan Plateau, Environ. Res. Lett., 6, 045403, https://doi.org/10.1088/1748-9326/6/4/045403, 2011.

Yi, S., He, Y., Guo, X., Chen, J., Wu, Q., Qin, Y., and Ding, Y.: The physical properties of coarse-fragment soils and their effects on permafrost dynamics: a case study on the central Qinghai–Tibetan Plateau, The Cryosphere, 12, 3067-3083, https://doi.org/10.5194/tc-12-3067-2018, 2018.

You, Y. H., Huang, C. L., Yang, Z. L., Zhang, Y., Bai, Y. L., and Gu, J.: Assessing Noah-MP Parameterization Sensitivity and Uncertainty Interval Across Snow Climates, J. Geophys. Res.-Atmos., 125, e2019JD030417, https://doi.org/10.1029/2019jd030417, 2020.

Yuan, W., Xu, W., Ma, M., Chen, S., Liu, W., and Cui, L.: Improved snow cover model in terrestrial ecosystem models over the Qinghai–Tibetan Plateau, Agric. For. Meteor., 218-219, 161-170, https://doi.org/10.1016/j.agrformet.2015.12.004, 2016.

Zeng, X., Wang, Z., and Wang, A.: Surface Skin Temperature and the Interplay between Sensible and Ground Heat Fluxes over Arid Regions, J. Hydrometeor., 13, 1359-1370, https://doi.org/10.1175/JHM-D-11-0117.1, 2012.

Zhang, G., Chen, F., and Gan, Y.: Assessing uncertainties in the Noah-MP ensemble simulations of a cropland site during the Tibet Joint International Cooperation program field campaign, J. Geophys. Res.-Atmos., 121, 9576-9596, https://doi.org/10.1002/2016jd024928, 2016.

Zhang, H., Su. Y., Jiang, H., Chao, H., and Su, W.: Influence of snow subliming process on land-atmosphere interaction at alpine wetland, J. Glaci. Geocry., 40, 1223-1230, 2018.

Zhang, T.: Influence of the seasonal snow cover on the ground thermal regime: An overview, Reviews of Geophysics, 43, RG4002, https://doi.org/10.1029/2004RG000157, 2005.

Zhao, L., Hu, G., Zou, D., Wu, X., Ma, L., Sun, Z., Yuan, L., Zhou, H., and Liu, S.: Permafrost changes and its effects on hydrological processes on Qinghai-Tibet Plateau, Bull. Chin. Acad. Sci., 34, 1233-1246, https://doi.org/10.16418/j.issn.1000-3045.2019.11.006, 2019.

Zheng, D., Van Der Velde, R., Su, Z., Wen, J., and Wang, X.: Assessment of Noah land surface model with various runoff parameterizations over a Tibetan river, J. Geophys. Res.-Atmos., 122, 1488-1504, https://doi.org/10.1002/2016jd025572, 2017.

Zheng, H., Yang, Z.-L., Lin, P., Wei, J., Wu, W.-Y., Li, L., Zhao, L., and Wang, S.: On the sensitivity of the precipitation partitioning into evapotranspiration and runoff in land surface parameterizations, Water Resour. Res., 55, 95-111, https://doi.org/10.1029/2017WR022236, 2019.

Zheng, W., Wei, H., Wang, Z., Zeng, X., Meng, J., Ek, M., Mitchell, K., and Derber, J.: Improvement of daytime land surface skin temperature over arid regions in the NCEP GFS model and its impact on satellite data assimilation, J. Geophys. Res.-Atmos., 117, D06117, https://doi.org/10.1029/2011jd015901, 2012.

Zilitinkevich, S.: Non-local turbulent transport pollution dispersion aspects of coherent structure of convective flows, Air Pollution III, Air pollution theory and simulation (H Power, N Moussiopoulos, C A Brebbia, eds) Computational Mechanics Publ , Southampton, Boston, 1, 53-60, 1995.

Zou, D., Zhao, L., Sheng, Y., Chen, J., Hu, G., Wu, T., Wu, J., Xie, C., Wu, X., Pang, Q., Wang, W., Du, E., Li, W., Liu, G., Li, J., Qin, Y., Qiao, Y., Wang, Z., Shi, J., and Cheng, G.: A new map of permafrost distribution on the Tibetan Plateau, The Cryosphere, 11, 2527-2542, https://doi.org/10.5194/tc-11-2527-2017, 2017.